

Layout Optimization of Binocular Stereo Vision Measuring System

Zhenyuan JIA, Mingxing LI, Wei LIU, Yang LIU and Zhiliang SHANG

Key Laboratory for Precision and Non-traditional Machining Technology
of the Ministry of Education, Dalian University of Technology,

116024, People's Republic of China

Tel.: +86-0411-84708159, fax: +86-0411-84708159

E-mail: lw2007@dlut.edu.cn

Received: 9 October 2013 /Accepted: 22 November 2013 /Published: 30 December 2013

Abstract: When measuring the dimensions of large parts with binocular stereo vision measuring system, image point extraction error, resulting from image sampling, is one of the key influencing factors to the measuring accuracy. In this paper, a mathematical model of the relationship between the measurement error caused by image point extraction error (resulting from image sampling) and structural parameters, such as focal length, baseline distance, etc. is proposed. In this model, the constraint of effective field of view (FOV) of the binocular sensor is taken into consideration. Then, the layout optimization is conducted by using the genetic algorithm (GA) to obtain a set of optimal structural parameters. Finally, both the comprehensive measurement error of the space points and their measurement error in each coordinate component are analyzed under the optimal layout. The analysis method proposed in this paper would provide effective theoretical guidance for the reasonable layout of the cameras without calibration. *Copyright © 2013 IFSA.*

Keywords: Binocular stereo vision, Extraction error, Structural parameters, Genetic algorithm, Layout optimization, Image sampling.

1. Introduction

Binocular stereo vision, as a non-contact measuring method with good real-time performance and high measuring accuracy, has been widely applied in many fields such as industrial detection, target identification, etc. Especially, binocular stereo vision measuring method has an incomparable advantage over other measuring methods in real-time measurement of geometrical dimensions for large parts during machining. Many studies have been conducted to obtain high-precision results using binocular stereo vision, however, most of them mainly focused on how to improve the accuracy of calibration and the precision of stereo matching.

Meanwhile, the effect of structural parameters (focal length, baseline distance and camera deflection angle) of the binocular stereo vision measuring system on the measuring accuracy is often overlooked. In fact, structural parameters not only determine the range of the effective field of view (FOV), but also affect the distribution of measurement errors. During the actual measurement, once the camera calibration is done, then the relative orientations of these two cameras should remain unchanged, that is, the structural parameters are fixed. Therefore, it is necessary to conduct layout optimization of binocular stereo vision system before camera calibration. A set of optimal structural parameters will be acquired to improve the measuring

accuracy. According to the error analysis theory, Y. B. Guo [1] and Q. Liu [2] established an error model of binocular stereo vision measuring system, and they observed the effect of every structural parameter one by one on the measurement accuracy. However, all the structural parameters had not been comprehensively considered. S. O. Mason [3] developed a layout optimization software based on expert system. However, it is not easy for inexperienced users to improve the quality of expert system by obtaining accurate and all-sided knowledge. D. Fritsch [4] used first-order design strategies to optimize the layout of cameras, whereas, this method can trap into local optimization easily. M. Saadatseresht [5] proposed a novel method based on the fuzzy logic reasoning strategy to improve the configuration of an existing photogrammetric network by adding additional imaging stations, and this work does not guarantee the global optimum for the camera placement. J. C. Chen [6] considered both the camera calibration and the uncertainty propagation during the three-dimensional reconstruction process of the spatial points, and the genetic algorithm (GA) was utilized to solve the layout optimization problem. However, intrinsic parameters of the cameras must be calibrated beforehand. This work is not aimed at the image point extraction error resulting from image sampling. So also is the research conducted by G. Olague [7], who presented a solution to the problem of optimal camera placement using the multi-cellular genetic algorithm (MGA).

The paper is organized as follows. In Section 2, some descriptions of the image point extraction error resulting from image sampling are given. In Section 3, the layout forms of the binocular stereo vision sensor are introduced. Then, a mathematical model of the relationship between the measurement error caused by image point extraction error (resulting from image sampling) and structural parameters is proposed in Section 4. In Section 5, the single objective optimization problem, which is transformed from the layout optimization problem, is solved by using the GA. Finally, some conclusions are discussed in Section 6.

2. Image Point Extraction Error Resulting from Image Sampling

An analog image, which is expressed with a continuous light intensity distribution function of the incident radiance, cannot be represented exactly in a digital computer. Hence, it is necessary to convert the analog image into a digital image by discretizing the analog image into a number of small square areas (called pixel) through some digital imaging device (e.g., digital cameras). The space discretization process is called image sampling. As to the pixel-precise localization of the feature points, we can only obtain the location information of the pixel where the

feature point lies. If we regard the coordinates of the pixel as the coordinates of that point, then, there will be image point extraction error resulting from image sampling. Supposed that the pixel size is denoted by $\delta \times \delta$ (length and width), then the maximal image point extraction error resulting from image sampling will be $\pm 0.5\delta$. We take the sampling process of a single point in an image for example, as shown in Fig. 1.

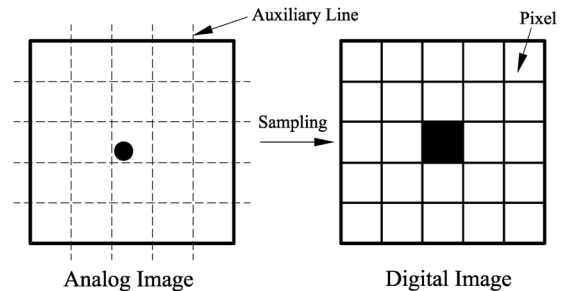


Fig. 1. Sampling process of a single point in the image.

It is noted that the measurement error mentioned below in this paper is referring to the measurement error caused by the image point extraction error, resulting from image sampling.

3. Layout Forms of the Binocular Stereo Vision Sensor

The symmetry layout of two cameras, assumed to have identical parameters, is investigated in this paper. According to the relative orientations of the optical axes of those two cameras, the binocular stereo vision measuring system can be classified into two types: parallel-optical-axis system and crossed-optical-axis system, as shown in Fig. 2.

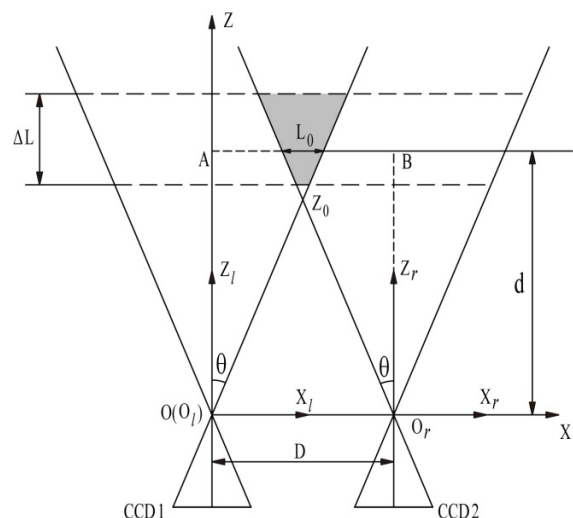


Fig. 2 (a). Layout forms of the binocular stereo sensor: parallel-optical-axis system ($\varphi = 0$).

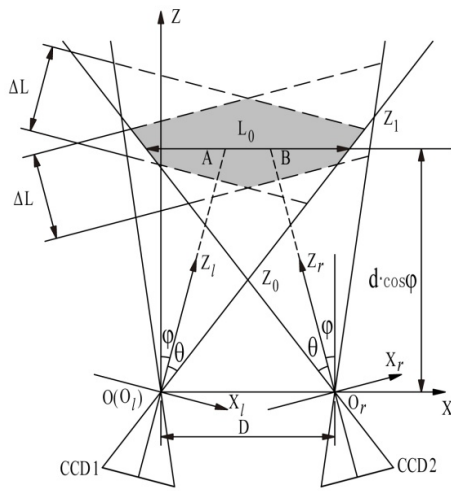


Fig. 2 (b). Layout forms of the binocular stereo sensor: crossed-optical-axis system ($\varphi > 0$).

The following notations are used: (a) $O_l X_l Y_l Z_l$ is the camera coordinate system (CCS) of the left vision sensor (CCD1), where O_l is the projection center of CCD1, $O_l Z_l$ is the optical axis of CCD1, and Y_l is one of the coordinate axes, which can be determined from X_l and Z_l with the right-hand rule. (b) $O_r X_r Y_r Z_r$ is the camera coordinate system (CCS) of the right vision sensor (CCD2), where O_r is the projection center of CCD2, $O_r Z_r$ is the optical axis of CCD2, and Y_r is one of the coordinate axes, which can be determined from X_r and Z_r with the right-hand rule. (c) $OXYZ$ is the world coordinate system (WCS), where O , coinciding with O_l , is the origin of the WCS. (d) D is the baseline distance, $d = |O_l A| = |O_r B|$ is the focus distance, and f is the focal length. (e) θ is the angle between the optical axis and the boundary line of the FOV, and φ is the angle between the optical axis and Z axis, i.e., the camera deflection angle. (f) Z_0 is the starting point of the overlap region of the FOV, and L_0 is the length of effective FOV at $Z = d$ (as shown in Fig. 2(a)) or $Z = d \cdot \cos \varphi$ (as shown in Fig. 2(b)).

The CCS is defined such that its x and y axes are parallel to the column and row axes of the image plane, respectively, and the z axis, perpendicular to the image plane, has the positive direction pointing to the front of cameras.

The effective FOV for binocular stereo vision measuring system is the overlapping FOV of the two cameras within the range of their depth of field (DOF), as shown by the shaded area in Fig. 2. The zone between dotted lines, which is denoted by ΔL , represents the DOF of the cameras. The object to be measured must stay within the effective FOV when using binocular stereo vision sensor. Hence, those studies, analyzing the effects of structural parameters

on the measurement error without regarding the constraint of the effective FOV, all have some limitation [1].

For ease of comparison, those two layout forms of the binocular stereo sensor are of the same baseline distance, as shown in Fig. 2. It can be clearly seen that the utilization rate of the FOV in parallel-optical-axis system is much less than that in crossed-optical-axis system. As to parallel-optical-axis system, a wide range of effective FOV can be gotten by significantly reducing the baseline distance. By contrast, as to crossed-optical-axis system, the layout of cameras is relatively free and a large baseline distance can be taken. Actually, measuring equipments in the workshop should be kept as compact as possible, so the baseline distance cannot be too large. However, when $\varphi > \theta$, there will be $L_0 < D$, so in most cases, the range of effective FOV cannot meet the requirements of dimension measurement for large parts. Therefore, analyses are conducted just for the crossed-optical-axis system ($0 < \varphi \leq \theta$) in this paper.

4. Mathematical Relationship Between the Measurement Error and Structural Parameters

The structural parameters of the binocular stereo vision measuring system mentioned in this paper include focal length f , baseline distance D and the angle φ between the optical axis and Z axis.

As illustrated in Fig. 3, the 3D coordinates of point P in the WCS is denoted by (X_w, Y_w, Z_w) , and its corresponding coordinates in the CCS of CCD1 and CCD2 are (X_l, Y_l, Z_l) and (X_r, Y_r, Z_r) , respectively. The image points of point P in the image planes of CCD1 and CCD2 are p_l and p_r , and their corresponding coordinates in the physics image coordinate system (in unit of millimeter) are (x_l, y_l) and (x_r, y_r) , respectively.

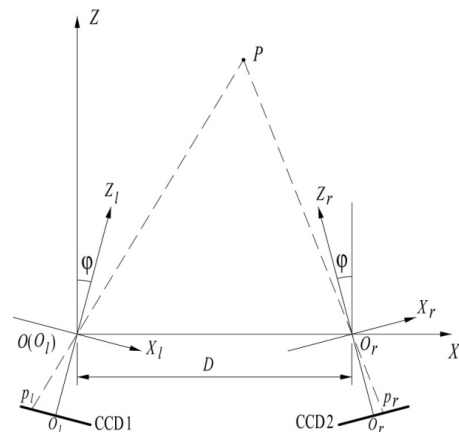


Fig. 3. The image points of point P in the image planes of two vision sensors.

For the pinhole camera model that describes the perspective projection from three dimensions to two dimensions, the following expressions that relate the coordinates of point P in the CCS and the coordinates in the physics image coordinate system are given by:

$$\begin{cases} x_l = f \frac{X_l}{Z_l} \\ y_l = f \frac{Y_l}{Z_l} \\ x_r = f \frac{X_r}{Z_r} \\ y_r = f \frac{Y_r}{Z_r} \end{cases} \quad (1)$$

The relationship between the coordinates in the CCS and the corresponding coordinates in the WCS can be expressed as the following simultaneous equations:

$$\begin{cases} X_l = X_w \cos \varphi - Z_w \sin \varphi \\ Y_l = Y_w \\ Z_l = Z_w \cos \varphi + X_w \sin \varphi \end{cases} \quad (2)$$

$$X_w = \frac{D \cdot (f \cos \varphi + x_r \sin \varphi) \cdot (f \sin \varphi + x_l \cos \varphi)}{(f \sin \varphi + x_l \cos \varphi) \cdot (f \cos \varphi + x_r \sin \varphi) + (f \sin \varphi - x_r \cos \varphi) \cdot (f \cos \varphi - x_l \sin \varphi)} \quad (5)$$

$$Y_w = \frac{D \cdot (x_r \sin \varphi - x_l \sin \varphi + 2f \cos \varphi)}{(f \sin \varphi + x_l \cos \varphi) \cdot (f \cos \varphi + x_r \sin \varphi) + (f \sin \varphi - x_r \cos \varphi) \cdot (f \cos \varphi - x_l \sin \varphi)} \cdot \frac{y_l y_r}{y_l + y_r} \quad (6)$$

$$Z_w = \frac{D \cdot (f \cos \varphi + x_r \sin \varphi) \cdot (f \cos \varphi - x_l \sin \varphi)}{(f \sin \varphi + x_l \cos \varphi) \cdot (f \cos \varphi + x_r \sin \varphi) + (f \sin \varphi - x_r \cos \varphi) \cdot (f \cos \varphi - x_l \sin \varphi)} \quad (7)$$

The above derivation process is built on the premise of perspective projection. However, owing to the image sampling, the corresponding image point of the point P with continuous distribution in 3D space is discrete in the image plane, so there are image point extraction errors [8-9]. As to those location methods with pixel accuracy, whose location accuracy is 0.5 pixels, the theoretical position of an image point deviates from the actual extraction result within ± 0.5 pixels. If we consider the case where the measurement error is maximal, then the image extraction errors in the left and right image planes will be:

$$\varepsilon_l = \varepsilon_r = \pm 0.5 \delta, \quad (8)$$

where $\delta \times \delta$ denotes the pixel size.

$$\begin{cases} X_r = (X_w - D) \cos \varphi + Z_w \sin \varphi \\ Y_r = Y_w \\ Z_r = Z_w \cos \varphi + (D - X_w) \sin \varphi \end{cases} \quad (3)$$

After substituting Equation (2) and Equation (3) into Equation (1), the relationship between the coordinates in the physics image coordinate system and the coordinates in the WCS can be represented by:

$$\begin{cases} x_l = f \frac{X_w \cos \varphi - Z_w \sin \varphi}{Z_w \cos \varphi + X_w \sin \varphi} \\ y_l = f \frac{Y_w}{Z_w \cos \varphi + X_w \sin \varphi} \\ x_r = f \frac{(X_w - D) \cos \varphi + Z_w \sin \varphi}{Z_w \cos \varphi + (D - X_w) \sin \varphi} \\ y_r = f \frac{Y_w}{Z_w \cos \varphi + (D - X_w) \sin \varphi} \end{cases} \quad (4)$$

The expression of the coordinates of point P in the WCS can be resolved from all the aforementioned equations:

Let $(\tilde{x}_l, \tilde{y}_l)$ and $(\tilde{x}_r, \tilde{y}_r)$ represent the actual extraction coordinates in the physics image coordinate system corresponding to the theoretical coordinates (x_l, y_l) and (x_r, y_r) . The relationship between the actual extraction coordinates and the theoretical coordinates is as follows:

$$\begin{cases} \tilde{x}_l = x_l + \varepsilon_l \\ \tilde{y}_l = y_l + \varepsilon_l \\ \tilde{x}_r = x_r + \varepsilon_r \\ \tilde{y}_r = y_r + \varepsilon_r \end{cases} \quad (9)$$

The actual 3D coordinates of point P in the WCS can be acquired from the actual extraction coordinates of the image point in the physics image coordinate system:

$$\tilde{X}_w = \frac{D \cdot (f \cos \varphi + \tilde{x}_r \sin \varphi) \cdot (f \sin \varphi + \tilde{x}_l \cos \varphi)}{(f \sin \varphi + \tilde{x}_l \cos \varphi) \cdot (f \cos \varphi + \tilde{x}_r \sin \varphi) + (f \sin \varphi - \tilde{x}_r \cos \varphi) \cdot (f \cos \varphi - \tilde{x}_l \sin \varphi)} \quad (10)$$

$$\tilde{Y}_w = \frac{D \cdot (\tilde{x}_r \sin \varphi - \tilde{x}_l \sin \varphi + 2f \cos \varphi)}{(f \sin \varphi + \tilde{x}_l \cos \varphi) \cdot (f \cos \varphi + \tilde{x}_r \sin \varphi) + (f \sin \varphi - \tilde{x}_r \cos \varphi) \cdot (f \cos \varphi - \tilde{x}_l \sin \varphi)} \cdot \frac{\tilde{y}_l \tilde{y}_r}{\tilde{y}_l + \tilde{y}_r} \quad (11)$$

$$\tilde{Z}_w = \frac{D \cdot (f \cos \varphi + \tilde{x}_r \sin \varphi) \cdot (f \cos \varphi - \tilde{x}_l \sin \varphi)}{(f \sin \varphi + \tilde{x}_l \cos \varphi) \cdot (f \cos \varphi + \tilde{x}_r \sin \varphi) + (f \sin \varphi - \tilde{x}_r \cos \varphi) \cdot (f \cos \varphi - \tilde{x}_l \sin \varphi)} \quad (12)$$

The mathematical model of the relationship between the measurement error Q and the structural parameters is set up:

$$Q = \sqrt{(\tilde{X}_w - X_w)^2 + (\tilde{Y}_w - Y_w)^2 + (\tilde{Z}_w - Z_w)^2} \quad (13)$$

5. Layout Optimization of the Binocular Stereo Vision Measuring System

5.1. Optimization Problem

In the dimension measuring system for large parts, the imaging devices are two monochrome CCD cameras (Princeton MegaPlus II ES4020) with a resolution of 2048×2048 pixels. Their active area of the camera view has the dimension of $15.2 \text{ mm} \times 15.2 \text{ mm}$ and the pixel size $\delta \times \delta$ is $7.4 \text{ mm} \times 7.4 \text{ mm}$. In order to meet the needs of different sizes of the FOV, the zoom lens (Tamron AF18-250 mm F/3.5-6.3 Di-II LD) with a focal range of 18-250 mm and an aperture range of $F/3.5 - F/6.3$ is selected. As the light rays passing the lens tube and the diaphragm, some may be diffracted. In general, the quality of a lens increases as diaphragm closes down before the proportion of the diffracted light and the non-diffracted light becomes too significant to be neglected. However, with a loss-pass filter (BD, 450SP) in front of each camera, the background light will be relatively weak, and hence a large aperture value $F/3.5$ is chosen here so as to capture clear images by allowing more light to strike the CCD plane. To avoid the damage of measuring devices, the measuring system is located at about 8000 mm away from the machining center, so the focus distance d can be set to 8000 mm in this paper.

According to the requirements of the actual dimension measurement for large parts, the size of effective FOV should meet the following limits: the length range (along the X axis) is $L \geq 3000$ mm, the width range (along the Z axis) is $W \geq 1000$ mm and the height range (along the Y axis) is $H \geq 3000$ mm, as shown in Fig. 4. In order to obtain a compact layout, and owing to the dimension limits of the cameras themselves and their mounting pedestals, the range of baseline distance is set to $100 \text{ mm} \leq D \leq 2000 \text{ mm}$.

In the XOZ plane, the angle between the optical axis and the boundary line of the FOV is computed as follows:

$$\theta = \arctan\left(\frac{\gamma}{2f}\right), \quad (14)$$

where γ represents the length or the width of the active area of the camera view, i.e., $\gamma=15.2$ mm.

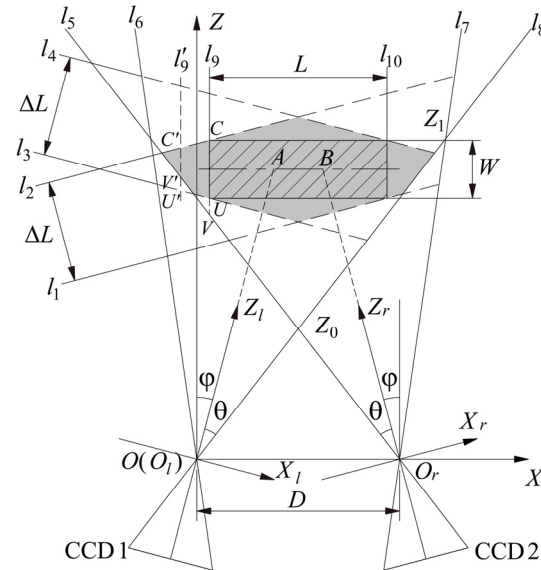


Fig. 4. Structural sketch map of the binocular stereo vision measuring system.

The zone of acceptable sharpness of an image is referred to as the depth of field (DOF), as shown in Fig. 5.

Front depth of field (F-DOF) is given by:

$$\Delta L1 = \frac{F \cdot CoC \cdot d^2}{f^2 + F \cdot CoC \cdot d}, \quad (15)$$

Rear depth of field (R-DOF) is given by:

$$\Delta L_2 = \frac{F \cdot CoC \cdot d^2}{f^2 - F \cdot CoC \cdot d}, \quad (16)$$

Depth of field (DOF) can be calculated as follows:

$$\Delta L = \Delta L_1 + \Delta L_2 = \frac{2f^2 \cdot F \cdot CoC \cdot d^2}{f^4 - F^2 \cdot CoC^2 \cdot d^2}, \quad (17)$$

where F represents the aperture value, and CoC represents the permissible circle of confusion, the CoC diameter limit may be given by the “Zeiss formula”, $CoC = a / 1730$, with a being the diagonal of the camera view (i.e. $15.2\sqrt{2} \text{ mm}$) [10]. Then the value of CoC can be calculated by:

$$CoC = 15.2\sqrt{2} / 1730 \text{ mm} = 0.0124 \text{ mm} \quad (18)$$

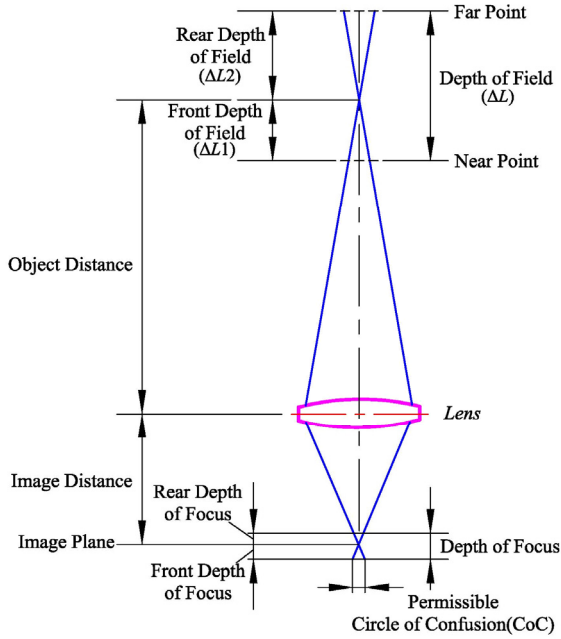


Fig. 5. Geometric interpretation of DOF and permissible CoC .

As illustrated in Fig. 4, the equations of those lines where the boundary lines of the DOF lie are formulated as follows:

$$l1: z = \tan \varphi \cdot (x - D) + \sec \varphi \cdot (d - \Delta L1) \quad (19)$$

$$l2: z = \tan \varphi \cdot (x - D) + \sec \varphi \cdot (d + \Delta L2) \quad (20)$$

$$l3: z = -\tan \varphi \cdot x + \sec \varphi \cdot (d - \Delta L1) \quad (21)$$

$$l4: z = -\tan \varphi \cdot x + \sec \varphi \cdot (d + \Delta L2) \quad (22)$$

The equations of those lines where the boundary lines of FOV lie are as follows:

$$l5: z = -\cot(\varphi + \theta) \cdot (x - D) \quad (23)$$

$$l6: z = \cot(\varphi - \theta) \cdot x \quad (24)$$

$$l7: z = -\cot(\varphi - \theta) \cdot (x - D) \quad (25)$$

$$l8: z = \cot(\varphi + \theta) \cdot x \quad (26)$$

The equations of those lines where the boundary lines of the measurement range (along the length direction) are as follows:

$$l9: x = D/2 - L/2 \quad (27)$$

$$l10: x = D/2 + L/2 \quad (28)$$

$C(C')$ is the intersection point between line $l9(l9')$ and line $l2$, $U(U')$ is the intersection point between line $l9(l9')$ and line $l3$, $V(V')$ is the intersection point between line $l9(l9')$ and line $l5$. There are two situations for the width of FOV, $W = |CU|$ and $W = |C'V'|$. There will be:

$$W = \min\{|CU|, |C'V'|\}, \quad (29)$$

where

$$|CU| = -L \tan \varphi + \Delta L \sec \varphi \quad (30)$$

$$|C'V'| = -\frac{(\tan \varphi + \cot(\theta + \varphi)) \cdot (D + L)}{2} + \sec \varphi \cdot (d + \Delta L2) \quad (31)$$

The measurement errors are not evenly distributed in the effective FOV. Without loss of generality, 180 points, which are distributed uniformly over the measuring space (the cuboid shadow area located at the center of the effective FOV, as shown in Fig. 6) with the size of $3000 \text{ mm} \times 1000 \text{ mm} \times 3000 \text{ mm}$ (length, width and height), are chosen as the test points. Those points are numbered by the following rules: the measuring space is divided into five equidistant test planes along the Z axis, and the distance between two adjacent test planes is $1000/4 = 250 \text{ mm}$. There are 36 points (6 rows and 6 columns, meanwhile, row coordinates increase downward and column coordinates to the right) evenly distributed in each test plane ($3000 \text{ mm} \times 3000 \text{ mm}$ in size). So we can let $P_{k,(i,j)}$ represent the test point at row i , column j of the test plane k . As a result, the values of X are $\{D/2 - 1500, D/2 - 900, D/2 - 300, D/2 + 300, D/2 + 900, D/2 + 1500\}$, the values of Y are $\{-1500, -900, -300, 300, 900, 1500\}$ and the values of Z are five values chosen in the range from $\frac{1000(z_C - d')}{z_C - z_U} + d'$ to $d' - \frac{1000(d' - z_U)}{z_C - z_U}$ or in the range from $\frac{1000(z_C - d')}{z_C - z_V} + d'$ to $d' - \frac{1000(d' - z_V)}{z_C - z_V}$ equidistantly, where

$$d' = d \cdot \cos \varphi \quad (32)$$

The Z coordinate of point $C(C')$ is:

$$z_C = -\tan \varphi \cdot (D + L) / 2 + \sec \varphi \cdot (d + \Delta L_2) \quad (33)$$

The Z coordinate of point $U(U')$ is

$$z_U = -\tan \varphi \cdot (D - L) / 2 + \sec \varphi \cdot (d - \Delta L_1) \quad (34)$$

The Z coordinate of point $V(V')$ is:

$$z_V = \cot(\theta + \varphi) \cdot (D + L) / 2 \quad (35)$$

When the length L is set to 3000mm there should be $|CU|_{L=3000} \geq 1000$ and $|CV|_{L=3000} \geq 1000$.

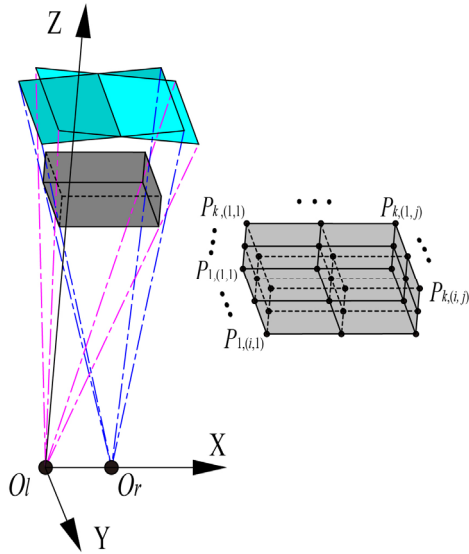


Fig. 6. Distribution of the test points.

Above all, the layout optimization problem can be translated into the single objective optimization problem with nonlinear inequality constraints and domain constraints (i.e., the lower and upper bounds for the optimization variables), as follows:

$$\left\{ \begin{array}{l} \min \Gamma = \left(\sum_{k=1}^5 \sum_{i=1}^6 \sum_{j=1}^6 Q_{k(i,j)} \right) / 180 \\ \text{s.t. } |CU|_{L=3000} \geq 1000 \\ |CV|_{L=3000} \geq 1000 \\ 18 \leq f \leq 250 \\ 0 < \varphi \leq \theta \\ 100 \leq D \leq 2000 \\ 0 \leq Z_0 < 8000 \\ \Delta L > 1000 \end{array} \right. , \quad (36)$$

where $Z_0 = D / (2 \tan(\theta + \varphi))$ and the optimization variables are those three structural parameters (f , D and φ). There should be a set of optimal

structural parameters which can minimize the measurement error.

5.2. The Genetic Algorithm (GA)

Most of the existing optimization methods, whose optimized results largely depend on the selection of initial values, are more likely to exhibit local search ability. However, the GA, which is based on the natural selection and natural inheritance in biosphere, is an effective heuristic stochastic search algorithm combining the survival-of-the-fittest mechanism in nature with the random exchange mechanism of chromosomes within groups. The GA has the ability in searching the entire solution space with more likelihood of finding the global optimum [11], for this reason, the GA is selected to solve the layout optimization problem of binocular stereo vision measuring system in this paper. The process of the GA is described as follows: the algorithm starts with a random initial population, then, the subsequent generation (called children) with good quality, which means a better solution to the optimization problem, is created from the current population (called parents) through genetic operators (selection, crossover and mutation). Next, such cycle of evolving process is repeated for multiple times until one of the stopping criteria is met.

Population size, encoding method, the method that each genetic operator adopts and stopping criteria, etc. all have a big impact on convergence speed and optimization result of the GA.

(a) Processing method of the constraints, design of the fitness function and the fitness scaling.

In this paper, as to the constrained optimization problem $F'_{obj}(x)$, processing methods of the constraints $c_i(x)$ ($i = 1, 2, \dots, m$) include rejecting method, repairing method and penalty method, where the penalty method seems to be the most popular. In this paper, the penalty method is used to convert the constrained optimization problem $F'_{obj}(x)$ into an unconstrained optimization problem $F_{obj}(x)$, as follows:

$$F_{obj}(x) = F'_{obj}(x) + M \sum_{i=1}^m c_i^+(x), \quad (37)$$

where M represents the penalty factor, the initial value of M is set to 10. When the problem is not solved to the required accuracy and those constraints are not satisfied, the penalty factor is increased by 100. $c_i^+(x)$ is defined by:

$$c_i^+(x) = \begin{cases} (c_i(x))^2, & c_i(x) > 0, \\ 0, & c_i(x) \leq 0, \end{cases} \quad i = 1, 2, \dots, m, \quad (38)$$

where $c_i(x)$ is the form of nonpositive inequality transformed from the constraints in Equation (36).

There is a one-to-one correspondence between the fitness function $F_{fit}(x)$ and the objective function $F_{obj}(x)$. Besides, the fitness function $F_{fit}(x)$ should meet the following requirements: the fitness value is nonnegative; the optimization direction of the objective function corresponds to the direction in which the fitness value increases. For the minimum optimization problem, the fitness function $F_{fit}(x)$ can be acquired by the following conversion from the objective function $F_{obj}(x)$ [12]:

$$F_{fit}(x) = \begin{cases} C_{\max} - F_{obj}(x), & \text{if } F_{obj}(x) < C_{\max} \\ 0, & \text{if } F_{obj}(x) \geq C_{\max} \end{cases}, \quad (39)$$

where C_{\max} is the relatively large number so as to ensure that $F_{fit}(x) \geq 0$.

As to the GA, the selection probability of each individual is determined by its corresponding fitness value. If just the expression of $F_{fit}(x)$ mentioned above is used to calculate the fitness values of the individuals, premature convergence and the random walk phenomena will occur easily. Therefore, a proper fitness scaling method should be used to enlarge or narrow the fitness values appropriately. Popular methods of fitness scaling include linear scaling, power law scaling, index scaling and rank scaling. Rank scaling method has the similar effects with other scaling methods, moreover, it can not only avoid selecting the scaling parameters [13], but also remove the effect of the spread of the raw fitness values. In this paper, the rank scaling method is adopted.

(b) Population size (PopSize).

PopSize is one of important factors affecting the performance of the GA. If PopSize is too small, performances of the GA will become poor for the absence of some valid genes. Large PopSize will help the GA cover a wide domain of possible solutions and effectively avoid the premature convergence. However, the larger the PopSize, the longer CPU time the GA will take. As to constrained problems, large PopSize should be selected to ensure that the feasible solutions within the population are enough.

(c) Encoding method.

The encoding method largely determines the efficiency of the genetic computation. Encoding methods include binary encoding, real-number encoding (i.e., float-point encoding), Gray encoding, and serial-number encoding, etc. Here, real-number encoding method should be adopted to improve the computational complexity and the computation precision of the GA [14]. The precision of the real-number encoding method, depending on the precision of the computer, is better than the other methods.

(d) Selection operator.

The main goal of selection operator is to avoid the deletion of useful genes, and to improve the computation efficiency and global convergence. Common methods of selection operator contain roulette wheel selection, tournament selection, stochastic universal sampling selection, remainder stochastic sampling selection and elitist selection, etc. Here, the stochastic universal sampling selection method is selected. The selection probability of each individual is proportional to its scaled value.

(e) Crossover operator and mutation operator.

A good collaboration between the crossover and the mutation, as two essential genetic operators to the GA, will make the algorithm obtain a better evolutionary performance. The crossover children are produced by recombining the genes of parents, while the mutation children are created by randomly changing the genes of individual parents. The values range of crossover probability P_c is usually from 0.6 to 1.0, and the values range of mutation probability P_m is usually from 0.005 to 0.01 [12]. Methods of the crossover operator mainly include one-point crossover, two-point crossover, scattered crossover, arithmetic crossover and uniform crossover. Here, the scattered crossover method is chosen. The principle of this method is to create a random binary vector, and produce a child by combining the genes where the vector is 1 from one parent with the genes where the vector is 0 from the other parent. Methods of the mutation operator mainly include simple mutation, uniform mutation, boundary mutation, non-uniform mutation, Gaussian mutation and adaptive feasible mutation. Adaptive feasible mutation is often chosen for constrained optimization problems [15]. The principle of this method is to randomly generate mutation directions by referring to the constraints of the optimization problem and the running state of the last iteration. That is, a self adaptation of mutation probability P_m is used. Next, we only consider how to determine a proper value of the crossover probability P_c .

(f) Stopping criteria.

In this paper, two criteria are used to determine when to terminate the GA: one is the number of iterations is equal to the maximum number of iterations, MaxGenera; the other is the weighted average change in the fitness value over a certain number of consecutive generations (ConGenera) is less than the function tolerance. The GA will stop as soon as either of the two stopping criteria is met.

For ease of comparison of the solution quality under different crossover probabilities P_c , a set of algorithm parameters, under which the GA is relatively easy to converge, was set as follows: PopSize (equal to 100), MaxGenera (equal to 400), ConGenera (equal to 100) and function tolerance (equal to 10^{-6}). P_c was set to increase from 0.6 to 1.0 with a step size of 0.01, then the GA was run ten

times for each value of P_c . The means and standard deviations of the best fitness value are shown in Fig. 7. All the experiments were conducted on the desktop with 1.98 GB of RAM and 2.53 GHz processor.

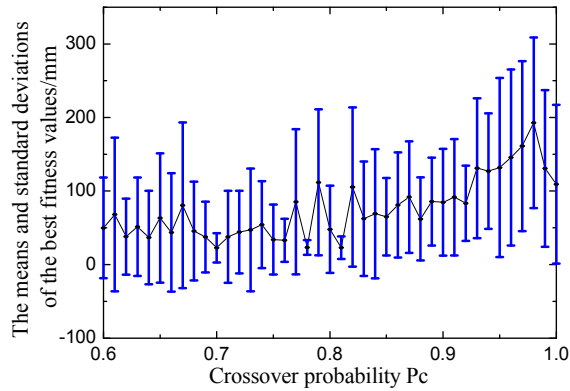


Fig. 7. The means and standard deviations of the best fitness values under different P_c .

As shown in Fig. 7, the choice of crossover probability has an apparent influence on the convergent results. The means and standard deviations of the best fitness values are less while the crossover probability P_c is equal to 0.7, 0.78 and 0.81. Then we compare the solution quality and speed of the GA under these three crossover probabilities, as listed in Table 1. By contrast, setting P_c to 0.78 is the right choice for the fitness function in this paper.

Table 1. Further comparison of the three crossover probabilities.

Items to be compared	$P_c = 0.7$	$P_c = 0.78$	$P_c = 0.81$
The mean value of the best fitness values /mm	22.767	23.350	23.129
The standard deviation of the best fitness value /mm	19.891	10.171	15.342
The mean value of time /s	1234.294	333.929	360.781

In order to get the global optimal solution, a much larger PopSize was selected and much higher stopping criteria were set. The parameters that the GA uses were set as follows: PopSize (equal to 500), MaxGenera (equal to 2000), ConGenera (equal to 500) and function tolerance (equal to 10^{-12}). Then the GA program was run several times, the results are listed in Table 2.

Table 2. Optimization results of the GA.

No.	Optimal solution			Optimal value/mm	CPU time/s
	f /mm	D /mm	φ /rad		
1	42.552	2000	0.103	5.834	10076.6
2	42.552	2000	0.103	5.834	10125.5
3	42.552	2000	0.103	5.834	10137.3
4	42.552	2000	0.103	5.834	10212.3

As shown in Table 2, the optimal solution to the optimization problem is: f equals to 42.552 mm, D equals to 2000 mm and φ equals to 0.103 rad (i.e., 5.92°); the optimal value is 5.834 mm; the mean value of CPU time is about 2.8 hours.

5.3. Error Analysis Under Optimal Parameter Settings

The placement of the binocular stereo vision measuring system is accomplished according to the optimal parameter settings (i.e., f equals to 42.552 mm, D equals to 2000 mm and φ equals to 5.92°). Then the comprehensive measurement error Q of those test points in different locations and the measurement error in each coordinate component (δX_w , δY_w and δZ_w) are observed, where

$$\begin{cases} \delta X_w = |\tilde{X}_w - X_w| \\ \delta Y_w = |\tilde{Y}_w - Y_w| \\ \delta Z_w = |\tilde{Z}_w - Z_w| \end{cases} \quad (40)$$

As shown in Fig. 8, the comprehensive measurement error of all the test points will increase with the measuring distance increasing along the Z axis. By comparing the comprehensive measurement error of test points in different test planes, we can see that the distributed regularity of the measurement error in each plane is identical. Take one of the test planes ($k=1$) for example, as shown in Fig. 9. The comprehensive measurement error is minimal in the center of the test plane, and the farther the test point is away from the center, the bigger the error is. The comprehensive measurement error is maximal at the four corners of the test plane. Likewise, take one of the test planes ($k=1$) for example, the measurement error in each coordinate component is shown in Fig. 10.

As shown in Fig. 10, the measurement error in Z_w coordinate component, which is much bigger than those in the other two coordinate components, changes little in the entire test plane. Whereas, the measurement error in X_w coordinate component is minimal in the center of X_w , i.e., the center of the baseline. Moreover, when the value of X_w is kept constant, the measurement error in X_w coordinate

component doesn't change with different values of Y_w . Similarly, the measurement error in Y_w coordinate component is minimal in the center of Y_w , and when the value of Y_w is kept constant, the measurement error in Y_w coordinate component changes little with different values of X_w .

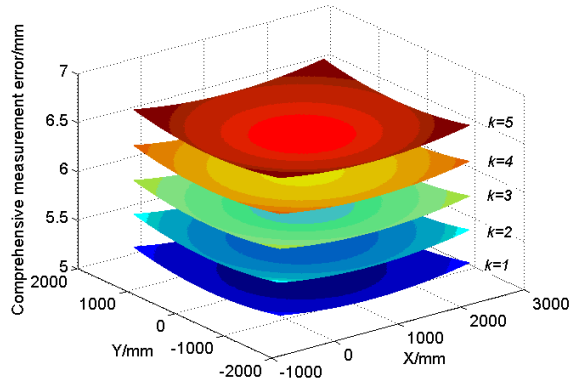


Fig. 8. The comprehensive measurement error of the test points in different locations.

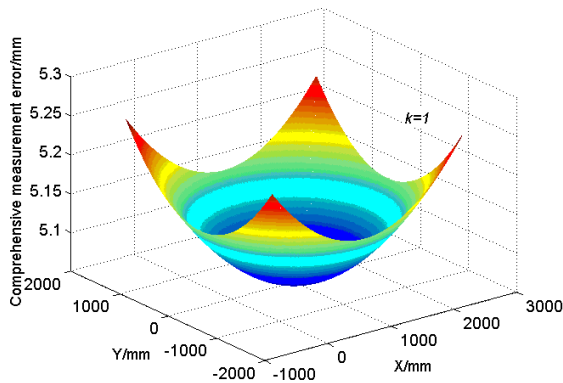


Fig. 9. The comprehensive measurement error of the test points in the test plane ($k=1$).

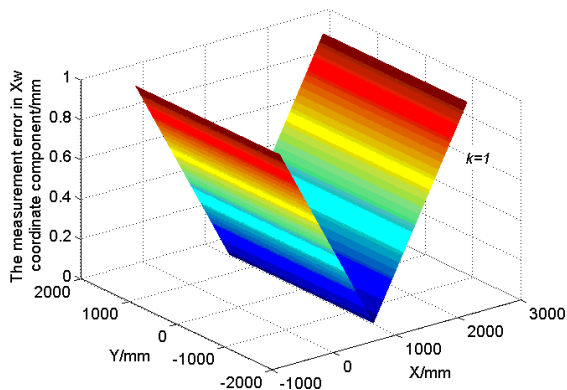


Fig. 10 (a). Measurement error in each coordinate component of the test points in different locations: in X_w coordinate component.

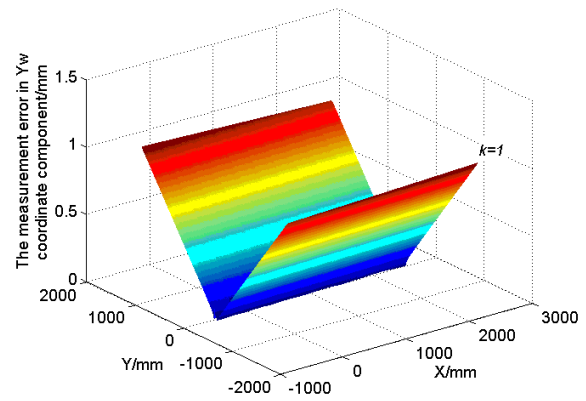


Fig. 10 (b). Measurement error in each coordinate component of the test points in different locations: in Y_w coordinate component

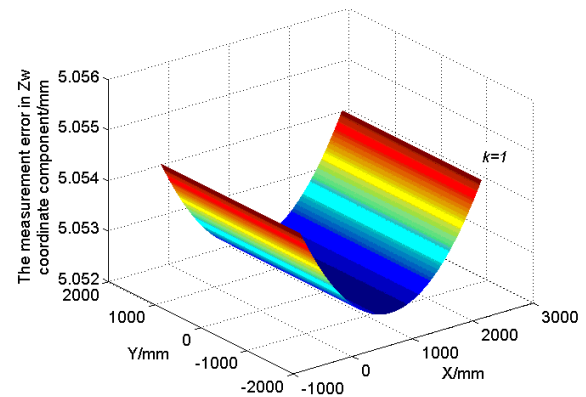


Fig. 10 (c). Measurement error in each coordinate component of the test points in different locations: in Z_w coordinate component.

5.4. Improvement of Measuring Accuracy

1) Increasing the baseline distance.

The optimal solution to the constrained objective optimization problem mention above is $[42.552 \ 2000 \ 0.103]$, i.e., when $f = 42.552 \text{ mm}$, $D = 2000 \text{ mm}$ and $\varphi = 0.103 \text{ rad}$, the objective function value is optimal. The value of D happens to be the upper bound of the value range of D , and based on that, some research is done to obtain some related rules by changing the upper bound of the value range of D . The parameters of the GA are set to: PopSize (equal to 500), MaxGenera (equal to 2000), ConGenera (equal to 500) and function tolerance (equal to 10^{-12}). The optimal solutions and optimal values under different value ranges of D are presented in Tab. 3.

As shown in Table 3, it can be clearly seen that the optimal value of D is always equal to the upper bound of the value range of D . So we can conclude that the measurement error will reduce with the increasing of the baseline distance. As a result, on the condition that the measuring system meets the

requirement of the layout on site, a longer baseline distance is more proper.

Table 3. The optimal solutions and optimal values under different value ranges of D .

Value range of D/mm	Optimal value /mm	Optimal solution [f/mm D/mm φ/rad]
$100 \leq D \leq 1500$	7.916	[41.799 1500 0.069]
$100 \leq D \leq 1600$	7.394	[41.957 1600 0.076]
$100 \leq D \leq 1700$	6.934	[42.111 1700 0.083]
$100 \leq D \leq 1800$	6.526	[42.261 1800 0.090]
$100 \leq D \leq 1900$	6.161	[42.408 1900 0.097]
$100 \leq D \leq 2000$	5.834	[42.552 2000 0.103]
$100 \leq D \leq 2100$	5.538	[42.693 2100 0.110]
$100 \leq D \leq 2200$	5.269	[42.830 2200 0.117]
$100 \leq D \leq 2300$	5.025	[42.964 2300 0.124]
$100 \leq D \leq 2400$	4.801	[43.096 2400 0.131]
$100 \leq D \leq 2500$	4.595	[43.224 2500 0.138]

2) Using the subpixel-precise extraction technology.

The above mentioned studies on the measurement error we have conducted so far are pixel-precise. Often, the subpixel-precise extraction technology, as an image processing tool, can make the resolution of the image become higher than a pixel. The accuracy of subpixel-precise location algorithms is generally 0.1~0.3 pixels, and in some ideal cases, the accuracy of some algorithms can even reach 0.01 pixels [16]. Assuming that the locating accuracy of subpixel-precise extraction technology is λ pixels, when we consider the case where the measurement error reaches the maximum, then the image extraction error of the left and right image plane is $\varepsilon_l = \varepsilon_r = \pm 0.5\lambda\delta$. Fig. 11 shows how the optimal value of the objective function changes as the accuracy grades of the location algorithms are varied.

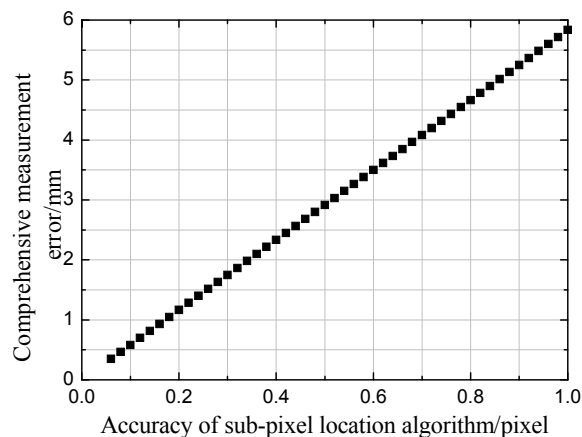


Fig. 11. The optimal value varies with the accuracy grade of the location algorithm.

Fig. 11 shows that there is a linear relationship between the comprehensive measurement error and

the accuracy grade of the subpixel-precise location algorithms. Furthermore, the measurement error can be reduced effectively by using the subpixel-precise extraction technology.

6. Conclusions

In this paper, a mathematical model of the relationship between the measurement error caused by image point extraction error (resulting from image sampling) and structural parameters, such as focal length, baseline distance, etc. was proposed. The GA is adopted to optimize the layout problem of the measuring system in which the cameras and lens have been given. Then, under the optimal parameter settings, the distributed regularities of the comprehensive measurement error and the measurement error in each coordinate component are analyzed. The comprehensive measurement error is minimal in the center of the test plane, and the farther the test point is from the center of the test plane, the bigger the error is. The measurement error in Z_w coordinate component is much bigger than those in the other two coordinate components. When measuring the dimensions of the large parts, the longer the baseline distance, the smaller the measurement error is. Furthermore, the measurement error will be effectively reduced by using some subpixel extraction technology. The research results in this paper will provide significant guidance and valuable reference for the proper layout of the binocular stereo vision measuring system.

Acknowledgements

This paper is supported by National Natural Science Foundation of China under Grant No. 51227004 and 51375075, and the Fundamental Research Funds for the Central Universities of China.

References

- [1]. Y. B. Guo, Y. Yao, Structural parameter optimization of binocular vision measuring system, *Infrared and Laser Engineering*, Vol. 35, Issue S1, 2006, pp. 506-509.
- [2]. Q. Liu, X. S. Qin, S. S. Ying and F. He, Structural parameter design and accuracy analysis of binocular vision measuring system, *China Mechanical Engineering*, Vol. 19, Issue 22, 2008, pp. 85-89.
- [3]. S. O. Mason, A. Grün, Automatic sensor placement for accurate dimensional inspection, *Computer Vision and Image Understanding*, Vol. 61, Issue 3, 1995, pp. 454-467.
- [4]. D. Fritsch, F. Crosilla, First-order design strategies for industrial photogrammetry, in *Proceedings of the International Conference on Society of Photo-Optical Instrumentation Engineers (SPIE)*, Orlando, Florida, 16-17 April 1990, pp. 432-438.

- [5]. M. Saadatseresht, F. Samadzadegan and A. Azizi, Automatic camera placement in vision metrology based on a fuzzy inference system, *Photogrammetric Engineering and Remote Sensing*, Vol. 71, Issue 12, 2005, pp. 1375-1385.
- [6]. J. C. Chen, L. P. Zhao and H. Zhang, Optimal placement of cameras for stereo-vision metrology, *Machine Tool and Hydraulics*, Vol. 40, Issue 15, 2012, pp. 34-37.
- [7]. G. Olague, R. Mohr, Optimal camera placement for accurate reconstruction, *Pattern Recognition*, Vol. 35, Issue 4, 2002, pp. 927-944.
- [8]. L. Yan, Z. X. Zhao and Y. Q. Zhou, Accuracy analysis and configuration design of stereo photogrammetry system based on CCD, *Chinese Journal of Scientific Instrument*, Vol. 29, Issue 2, 2008, pp. 410-413.
- [9]. H. B. Li, W. J. Shan and B. Liu, Research of error model on two eyes stereoscopic measurement system, *Optical Technique*, Vol. 32, Issue 1, 2006, pp. 24-26, 30.
- [10]. A. N. Belbachir, P. M. Göbel, Smart cameras: a historical evolution, A. N. Belbachir, *Springer US*, 2010.
- [11]. J. Holland, Adaptation in Natural and Artificial Systems, J. Holland, *The MIT Press*, Cambridge, 1992.
- [12]. M. Q. Li, J. S. Kou, D. Lin and S. Q. Li, Basic theory and application of genetic algorithm, S. Y. Wang, X. G. Yang, *Science Press*, Beijing, 2002.
- [13]. C. Reeves, Diversity and diversification in genetic algorithms: Some connections with tabu search, in *Proceedings of the International Conference on Artificial Neural Nets and Genetic Algorithms (ANNGA'93)*, Vienna, Austria, 14-16 April 1993, pp. 344-351.
- [14]. M. Gen, R. W. Cheng, Genetic algorithms and engineering optimization, H. R. Parsaei, *John Wiley & Sons*, 2000.
- [15]. W. Liu, The optimize design of ribbed plate retaining wall with anchors base on genetic algorithm, *Chongqing University*, Chongqing, 2008.
- [16]. Q. F. Yu, Y. Shang, Videometrics: principles and researches, D. P. Yan, J. Zhang, *Science Press*, Beijing, 2009.

2013 Copyright ©, International Frequency Sensor Association (IFSA). All rights reserved.
(<http://www.sensorsportal.com>)

SMITHERS APEX

IS 2014

FOCUS ON DIGITAL IMAGING

Save 10% Quote IF10AD

'The most productive single event we take part in in Europe - excellent return on investment'
Paul Double, EDA Solutions

18-20 March 2014
Park Plaza Victoria | London, UK

www.image-sensors.com